

Machine learning protocol to identify pairing symmetries via quasiparticle interference imaging in Ising superconductors

Adam Hložný,¹ Jozef Haniš,² Martin Gmitra,^{2,3,4} and Marko Milivojević^{1,5}

¹*Institute of Informatics, Slovak Academy of Sciences, 84507 Bratislava, Slovakia*

²*Institute of Experimental Physics, Slovak Academy of Sciences, 04001 Košice, Slovakia*

³*Institute of Physics, Pavol Jozef Šafárik University in Košice, 04001 Košice, Slovakia*

⁴*New Technologies Research Centre, University of West Bohemia, Univerzitní 8, CZ-301 00 Pilsen, Czech Republic*

⁵*Faculty of Physics, University of Belgrade, 11001 Belgrade, Serbia*

(Dated: February 24, 2026)

Identifying the pairing symmetry in unconventional superconductors is essential for reliably characterizing their superconducting states and for enabling their integration into realistic quantum devices. Here, we introduce a machine-learning-guided strategy to determine pairing symmetry from quasiparticle interference (QPI) data, which integrates first-principles calculations, tight-binding modeling, and symmetry-based classification of the superconducting pairing function. We demonstrate the approach on monolayer NbSe₂ as an experimentally accessible probe of superconductivity in real materials, within a single scalar-impurity Bogoliubov–de Gennes framework. Our analysis shows that the QPI-to-parameter inverse problem can be solved with high accuracy for most superconducting pairing channels in this setting, indicating that QPI carries rich, learnable information about the superconducting gap structure. Taken together, these results demonstrate that machine-learning-assisted QPI analysis provides a promising pathway for precise learning of superconducting pairing functions in quantum materials.

I. INTRODUCTION

The experimental identification of pairing symmetry in unconventional superconductors [1–3] is crucial for understanding the fundamental mechanisms behind superconductivity and for guiding the design of materials with novel quantum properties. This determination remains a central challenge in condensed matter physics due to the subtle and complex nature of the superconducting order parameter [4, 5]. Techniques like Josephson junction measurements and momentum-resolved gap spectroscopy often face difficulties isolating intrinsic superconducting signals from material-specific scattering and quasiparticle interference effects [6–8]. This challenge is especially pronounced in more complex systems such as cuprates and iron-based superconductors, where the exact nature of the pairing symmetry is still debated [5, 9]. Current proposals range from nodal d-wave to anisotropic s-wave. Addressing these controversies requires advanced, robust symmetry-informed methodologies capable of describing the momentum-dependent pairing functions that capture both the detailed k-space structure and the possible mixing of singlet and triplet components in the superconducting gap. This refined understanding is essential for progressing toward the unambiguous identification of unconventional superconducting states.

The key to detecting the nature of superconductivity, and its topological character, lies in understanding the nature of the Cooper pairs, which are the fundamental building blocks of the superconducting state. This understanding can be achieved by analyzing quasiparticle interference (QPI), a phenomenon where quasiparticles scatter off defects or boundaries, resulting in spa-

tial modulations of the local density of states that are captured in QPI spectra. While QPI patterns [10–16], measurable via techniques like scanning tunneling microscopy (STM) [17–19], can reveal signatures of superconducting pairing [20, 21], extracting and interpreting all the relevant information is a complex and challenging task [22]. This complexity limits unambiguous identification of pairing symmetries in real materials and motivates usage of methods that are able to process large amounts of data.

Generating large datasets of QPI spectra through numerical simulations within the Bogoliubov–de Gennes (BdG) formalism offers a promising route to bridge the gap between theory and experiment. These simulations produce rich QPI patterns that capture subtle signatures of different superconducting pairing symmetries [23]. However, the vast complexity and volume of these data demands advanced analytical tools. Machine learning approaches [24], such as convolutional neural networks (CNNs), have demonstrated powerful capabilities for pattern recognition [25] in images such as the QPI patterns, opening avenues for high-accuracy classification of pairing symmetries and extraction of hidden superconducting parameters from both simulated and experimental QPI spectra [26]. Thus, combining symmetry-based classification with machine learning-assisted QPI analysis provides a transformative approach to uncovering the detailed nature of unconventional superconductivity in layered materials.

To address this, we introduce a machine-learning-guided scheme that integrates first-principles calculations, tight-binding modeling, and symmetry-based classification of superconducting pairing functions [27, 28],

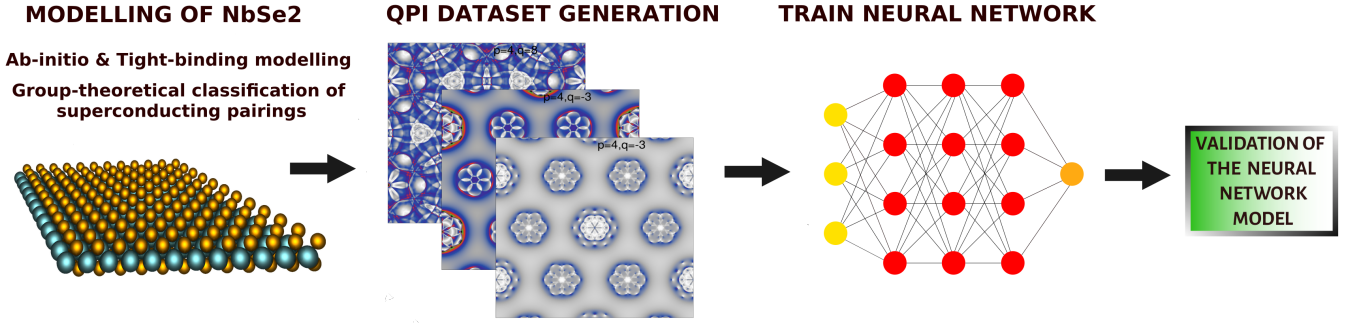


Figure 1. *Schematic overview of the proposed workflow.* Ab-initio calculations and tight-binding approach are used to model the normal phase of NbSe₂, whereas the superconducting pairing functions of NbSe₂ are determined using the group-theory approach. Secondly, a large dataset of simulated QPI spectra is generated across different superconducting parameters. This dataset is then used to train and optimize a neural network model.

using QPI imaging as an experimentally accessible probe in real quantum materials. We demonstrate its usefulness on monolayer NbSe₂ [29–31], revealing how this machine learning-assisted QPI analysis provides a robust pathway for precisely determining pairing symmetries across diverse unconventional superconductors that can be described using the BdG formalism.

This paper is organized as follows. In Section II, we provide theoretical framework for the analysis of superconductivity parings in monolayer NbSe₂ based on BdG formalism, QPI imaging and machine learning. In Section III, we present our machine-learning-based results of subtracting superconducting pairing information directly from simulated QPI images of monolayer NbSe₂. Using a two-head CNN, we simultaneously classify the superconducting pairing type (classified according to the irreducible representation of the group of monolayer NbSe₂) and extract the parameters controlling the superconducting state, such as the singlet–triplet mixing and gap magnitude. Finally, in Section IV, we present our conclusions.

II. THEORETICAL FRAMEWORK: SUPERCONDUCTIVITY, QPI, AND MACHINE LEARNING

To fully describe and analyze superconductivity in NbSe₂ using quasiparticle interference imaging and machine learning methods, we first describe details of the monolayer NbSe₂ model in its normal state, followed by the description of possible superconducting pairing withing the single-band approximation of free-standing monolayer NbSe₂. As a second step, we provide the theoretical framework to generate QPI images based on scalar impurity, implementing different types of superconducting pairing function previously defined. Finally, we provide a machine-learning-based protocol, based on convolutional neural network, able to analyze QPI images and solve the inverse problem of determining the supercon-

ducting pairing type and other microscopical details of the superconducting pairings.

A. Bogoliubov-de Gennes description of superconductivity in monolayer NbSe₂

We are interested in studying the effects of electron superconducting pairing in free-standing monolayer NbSe₂, having the D_{3h} symmetry, at a low-temperature regime. We model the superconductivity by the BdG formalism with the Hamiltonian

$$\mathcal{H}_{\text{BdG}} = \frac{1}{2} \sum_{\mathbf{k}} \Psi_{\mathbf{k}}^{\dagger} \mathcal{H}_{\mathbf{k}}^{\text{BdG}} \Psi_{\mathbf{k}}, \quad (1)$$

considering the Nambu spinor, $\Psi_{\mathbf{k}}^{\dagger} = [c_{\mathbf{k}\uparrow}^{\dagger}, c_{\mathbf{k}\downarrow}^{\dagger}, c_{-\mathbf{k}\uparrow}, c_{-\mathbf{k}\downarrow}]$ with fermionic creation $c_{\mathbf{k}\uparrow}^{\dagger}$ and annihilation $c_{-\mathbf{k}\uparrow}$ operators. The 4×4 BdG Hamiltonian in reciprocal space $\mathcal{H}_{\mathbf{k}}^{\text{BdG}}$ reads [32]

$$\mathcal{H}_{\mathbf{k}}^{\text{BdG}} = \begin{pmatrix} H_e(\mathbf{k}) & \Delta_{\mathbf{k}} \\ \Delta_{\mathbf{k}}^{\dagger} & -H_e^T(-\mathbf{k}) \end{pmatrix}, \quad (2)$$

where the electron-like Hamiltonian $H_e(\mathbf{k})$ is the effective tight-binding Hamiltonian

$$H_e(\mathbf{k}) = \mathcal{H}_{\text{orb}}(\mathbf{k}) + \mathcal{H}_I(\mathbf{k}), \quad (3)$$

In the equation above, the single-orbital part \mathcal{H}_{orb} describes the dispersion of the effective Nb d -band in the vicinity of the Fermi level [23, 33]

$$\begin{aligned} \mathcal{H}_{\text{orb}}(\mathbf{k}) = & \varepsilon_0 + 2t_1 f(\alpha, \beta) \\ & + 2t_2 (\cos 2\beta + 2 \cos 3\alpha \cos \beta) + 2t_3 f(2\alpha, 2\beta) \\ & + 4t_4 (\cos \alpha \cos 3\beta + \cos 4\alpha \cos 2\beta + \cos 5\alpha \cos \beta) \\ & + 2t_5 f(3\alpha, 3\beta) + 2t_6 (\cos 2\beta + 2 \cos 3\alpha \cos \beta) \\ & + 4t_7 (\cos 7\alpha \cos \beta + \cos 5\alpha \cos 3\beta + \cos 2\alpha \cos 4\beta), \end{aligned} \quad (4)$$

where $f(\alpha, \beta) = \cos 2\alpha + 2 \cos \alpha \cos \beta$, $\alpha = k_x a/2$, $\beta = \sqrt{3} k_y a/2$, a is the lattice constant, k_x and k_y are

components of the wave vectors in Cartesian frame, ε_0 is the chemical potential of the NbSe₂ monolayer, and t_i , $i = 1, \dots, 7$ are the real hopping parameters. The model describes Nb d -band close to the Fermi level up to 7-th neighbors.

In addition to the orbital part, one has to include the intrinsic spin-orbit coupling. The intrinsic spin-orbit coupling Hamiltonian H_I [33] up to the third neighbor equals to

$$\mathcal{H}_I(\mathbf{k}) = 2\sigma_z \left(\lambda_I^{(1)} g(\alpha, \beta) + \lambda_I^{(3)} g(2\alpha, 2\beta) \right), \quad (5)$$

where $g(\alpha, \beta) = \sin 2\alpha - 2 \sin \alpha \cos \beta$, σ_z is the Pauli matrix, and the nonzero real parameters $\lambda_I^{(1)}$ and $\lambda_I^{(3)}$ quantify the strength of the interaction in the first and third neighbor approximation. The parameter $\lambda_I^{(2)} = 0$ due to vertical mirror plane symmetry.

Finally, $\Delta_{\mathbf{k}}$ represents \mathbf{k} -dependent superconducting order parameter. Without entering into a macroscopic details of the superconductivity generation in a monolayer NbSe₂, it is possible to construct all allowed types of superconducting order parameters allowed by the \mathbf{D}_{3h} symmetry, divided into one singlet and two distinct triplet channels (parametrized by the spin pairing functions, $d_0 \propto (|\uparrow\downarrow\rangle - |\downarrow\uparrow\rangle)$ for singlet, and two triplet channels; one constructed by the $d_z \propto (|\uparrow\downarrow\rangle + |\downarrow\uparrow\rangle)$ triplet and one by two spin (d_x, d_y) (d_x, d_y) $\propto (|\uparrow\uparrow\rangle - |\downarrow\downarrow\rangle, |\uparrow\uparrow\rangle + |\downarrow\downarrow\rangle)$ and classified according to the irreducible representations (IRs) of the \mathbf{D}_{3h} group: one-dimensional (1D) IRs A_1^u , A_1^g , A_2^u , A_2^g , and two-dimensional (2D) IRs E^u and E^g . In Appendix A, we provide explicit forms of the superconducting gap functions classified according to IRs and the channel type: (s) for a singlet, (t, z) for a triplet constructed using the d_z spinor solely, and (t, xy) for a triplet constructed using (d_x, d_y) multiplet.

It is physically reasonable to assume that a singlet-triplet mixing can occur since for each IR both the singlet and triplet functions can be realized. By taking into account that the triplet function d_{xy} can not be mixed with the singlet and triplet function d_z due to the opposite parity with respect to the horizontal mirror plane symmetry, we can obtain the following mixed gap functions that transform according to one-dimensional IRs

$$\Delta_{A_1^u, \mathbf{k}} = \Delta \Delta_{A_1^u, \mathbf{k}}^{(t, xy)}, \quad (6)$$

$$\Delta_{A_2^u, \mathbf{k}} = \Delta \Delta_{A_2^u, \mathbf{k}}^{(t, xy)}, \quad (7)$$

$$\Delta_{A_1^g, \mathbf{k}} = \Delta (\cos \theta \Delta_{A_1^g, \mathbf{k}}^{(s)} + \sin \theta \Delta_{A_1^g, \mathbf{k}}^{(t, z)}), \quad (8)$$

$$\Delta_{A_2^g, \mathbf{k}} = \Delta (\cos \theta \Delta_{A_2^g, \mathbf{k}}^{(s)} + \sin \theta \Delta_{A_2^g, \mathbf{k}}^{(t, z)}), \quad (9)$$

where Δ is the order parameter magnitude. As one can notice, in the case of the 1D IRs A_1^u and A_2^u no mixing occurs, whereas in the case of 1D IRs A_1^g and A_2^g there is only one mixing parameter.

In the case of the 2D IRs the situation becomes more complicated since for each spin channel c , $c =$

(s), (t, z), (t, xy), gap function $\Delta_{E^{g/u}, \mathbf{k}}$ that transforms according to the IR $E^{g/u}$ can be written as $(\cos \theta_c \Delta_{E_1^{g/u}, \mathbf{k}}^c + e^{i\varphi_c} \sin \theta_c \Delta_{E_2^{g/u}, \mathbf{k}}^c)$, where $\Delta_{E_{1/2}^{g/u}, \mathbf{k}}^c$ are the two (real) components of the 2D IR $E^{g/u}$ for spin channel c , θ_c represents the component mixing parameter, whereas φ_c is time-symmetry breaking parameter. In addition to this, similar as in IRs A_1^g and A_2^g , for IR E^g there is a possibility of (s) and (t, z) spin channel mixing, giving rise to the most general form of gap functions (for more details, see Appendix A)

$$\Delta_{E^u, \mathbf{k}} = \Delta (\cos \theta_t \Delta_{E_1^u, \mathbf{k}}^{(t, xy)} + e^{i\varphi_t} \sin \theta_t \Delta_{E_2^u, \mathbf{k}}^{(t, xy)}),$$

$$\Delta_{E^g, \mathbf{k}} = \Delta \left[\cos \theta (\cos \theta_s \Delta_{E_1^g, \mathbf{k}}^{(s)} + e^{i\varphi_s} \sin \theta_s \Delta_{E_2^g, \mathbf{k}}^{(s)}) + \sin \theta (\cos \theta_t \Delta_{E_1^g, \mathbf{k}}^{(t, z)} + e^{i\varphi_t} \sin \theta_t \Delta_{E_2^g, \mathbf{k}}^{(t, z)}) \right],$$

However, in generating our large QPI dataset, we neglect the influence of parameters $\varphi_{s/t}$ for the reasons explained in Sec. III. To keep the analysis conceptually simple and demonstrate that our machine-learning protocol can determine key microscopic parameters of the superconducting Hamiltonian, we restrict the E^g representation to the singlet channel only. Therefore, the gap functions going to be used in the case of IRs E^u and E^g are

$$\Delta_{E^u, \mathbf{k}} = \Delta (\cos \theta \Delta_{E_1^u, \mathbf{k}}^{(t, xy)} + \sin \theta \Delta_{E_2^u, \mathbf{k}}^{(t, xy)}), \quad (10)$$

$$\Delta_{E^g, \mathbf{k}} = \Delta (\cos \theta \Delta_{E_1^g, \mathbf{k}}^{(s)} + \sin \theta \Delta_{E_2^g, \mathbf{k}}^{(s)}), \quad (11)$$

where in both cases, for simplicity, the component mixing parameter is given as θ .

B. Quasiparticle interference details

QPI imaging, typically performed via Fourier-transform scanning tunneling spectroscopy, has emerged as a powerful tool for probing superconducting states in quantum materials, offering momentum-resolved insights into Bogoliubov quasiparticle scattering that complement angle-resolved photoemission spectroscopy. In superconductors, QPI patterns arise from interference between incoming and elastically backscattered quasiparticles off impurities or defects, with the local density of states (LDOS) modulation dispersing according to the joint density of states on the BdG quasiparticle spectrum. Up to now, QPI has been positioned as a tool that can explain superconductivity in different systems [34, 35], being able to identify superconducting gap features such as phase structure, sign [36, 37] and orbital order [38].

Theoretical modeling of QPI in superconductors draws inspiration from the intuitive picture of a solid-state system as a sea of quasiparticles—wave-like excitations governed by the system's Hamiltonian. Small perturbations from impurities or crystal defects scatter these waves, creating standing wave modulations in the LDOS that

scanning tunneling spectroscopy (STS) directly visualizes through conductance maps. In the superconducting state, these become Bogoliubov quasiparticle interferences, where elastic scattering mixes electron- and hole-like excitations, encoding the momentum-space structure of the superconducting gap.

The T-matrix formalism provides a framework to compute these patterns theoretically, starting from the bare Green's function of the unperturbed Hamiltonian and re-summing scattering events off a localized impurity potential. Since quasiparticle responses of many impurities possess identical poles as a single impurity case [39, 40], we can approximate the description of the elastic scattering process via a spin-conserving single impurity. Such impurity potential can be written in real Nambu space as $V = v\tau_3 \otimes \sigma_0$, where v is the impurity strength, τ_3 is the Pauli matrix for electron-holes and σ_0 is the identity operator in the spin space. Considering the potential V as a perturbation, the LDOS can be calculated using the T-matrix approach via Green's function written as $G(\mathbf{k}, \mathbf{k}'; \omega) = G_0(\mathbf{k}, \mathbf{k}'; \omega) + \delta G(\mathbf{k}, \mathbf{k}'; \omega)$, where $G_0(\mathbf{k}, \mathbf{k}'; \omega)$ is retarded bare Green's function. The correction $\delta G(\mathbf{k}, \mathbf{k}'; \omega)$ can be found with the help of the T-matrix, which solves the scattering problem for a single scalar impurity [41]. Here, $\omega = \epsilon + i\delta$ corresponds to quasiparticle energy with small lifetime broadening ($\delta \approx 0.1$ meV). The spin-conserving scalar impurity V leads to a T-matrix, $T(\omega) = V \cdot [\mathbb{1} - V \cdot G_0(\omega)]^{-1}$, where $G_0(\omega) = 1/\Omega \int [\omega - \mathcal{H}_{\mathbf{k}}^{\text{BdG}}]^{-1}$ is the integrated bare Green's function within the first Brillouin zone (BZ). The scattered quasiparticle amplitude is equal to

$$\rho(\mathbf{q}; \omega) = -\frac{1}{\pi} \text{Im} \left\{ \frac{1}{\Omega} \int d\mathbf{k} \delta G(\mathbf{k}, \mathbf{k} + \mathbf{q}; \omega) \right\}, \quad (12)$$

in which the relation $\mathbf{k}' = \mathbf{k} + \mathbf{q}$ is used, with δG integrated over all possible \mathbf{k} points in the first BZ. The convolution theorem [42] enables efficient evaluation of QPI images $\rho(\mathbf{q}; \omega)$, reducing computational complexity and allowing analysis of fine-grid maps with minimal broadening. Spectral characteristics of the band structure are calculated using the imaginary part of the spectral function (for more details, see [23]).

C. Machine-learning details

After preparing a dataset of simulated QPI images (~ 5000 train samples, ~ 250 validation samples and ~ 250 test samples, equal number of samples per IR, the final step is to train a convolutional neural network to solve the inverse problem: from a QPI pattern to the underlying parameters of the effective BdG description (IR label and continuous Hamiltonian parameters). We adopt a multi-task setting with two prediction heads: (i) a classification head that predicts the superconducting irreducible representation (IR), and (ii) a regression head that predicts

the continuous parameters controlling the superconducting state.

Our primary model is based on a VGG-like architecture [43, 44], see Appendix B for details. Specifically, we use the convolutional *features* block of VGG16 as a shared backbone and modify the input layer to accept single-channel QPI maps by replacing the first convolution with a $1 \rightarrow 64$ kernel of size $k \times k$ (default $k = 3$), initialized with He/Kaiming normalization [45]. The resulting feature tensor is mapped to a fixed spatial size via adaptive average pooling to 7×7 , flattened, and passed through a fully connected aggregation layer,

$$\text{agg} = \text{ReLU}(W\mathbf{x} + \mathbf{b}), \quad (13)$$

where \mathbf{x} is flattened output of the convolutional feature extractor, W is weight matrix of the layer, \mathbf{b} is bias term and ReLU is defined as:

$$\text{ReLU}(t) = \max(0, t). \quad (14)$$

From this shared representation, two parallel heads are evaluated: (i) a classification head producing a score/probability vector over IRs, and (ii) a regression head producing four continuous outputs. In addition to this VGG-based model, we implemented an analogous modification of ConvNeXt [46]; however, for the present task and dataset size, the simpler VGG-based backbone provided more stable training and similar or marginally better overall validation performance.

The classification target is the IR label of the superconducting order parameter used to generate the QPI image. The regression target consists of the chemical potential μ , superconducting gap magnitude Δ , and the mixing angle θ entering gap functions in Eqs. (8)-(11). To avoid discontinuities associated with the periodicity of the mixing angle, we do not predict θ directly. Instead, we predict the two-component embedding

$$(\theta_1, \theta_2) = (\sin 2\theta, \cos 2\theta), \quad (15)$$

which correctly enforces the physical periodicity $\theta \equiv \theta + \pi$ in our problem (see the discussion in the next Section for further explanation). At inference, θ is reconstructed by $\theta = \frac{1}{2} \text{atan2}(\theta_1, \theta_2)$ (modulo π), where atan2 is arc tangent of θ_1/θ_2 with proper choice of quadrant. The model is trained with a weighted multi-task objective function,

$$\mathcal{L} = w_{\text{IR}} \mathcal{L}_{\text{CE}}(\hat{\mathbf{p}}, \mathbf{y}_{\text{IR}}) + w_{\text{param}} \|\hat{\mathbf{r}} - \mathbf{y}_{\text{param}}\|^2, \quad (16)$$

where $\hat{\mathbf{p}}$ denotes the predicted IR scores/probabilities, \mathbf{y}_{IR} one-hot encoded IR ground truths, $\hat{\mathbf{r}} = (\hat{\theta}_1, \hat{\theta}_2, \hat{\mu}, \hat{\Delta})$ predicted parameters of the BdG Hamiltonian, and $\mathbf{y}_{\text{param}}$ the corresponding ground-truth targets. Furthermore, $w_{\text{IR}}, w_{\text{param}}$ are weights of the IR and BdG parameter parts of the objective function, with \mathcal{L}_{CE} denoting categorical cross-entropy defined as:

$$\mathcal{L}_{\text{CE}}(\hat{\mathbf{p}}, \mathbf{y}_{\text{IR}}) = - \sum_{i=1}^K (\mathbf{y}_{\text{IR}})_i \log \hat{p}_i, \quad (17)$$

with summation running across possible IRs. The loss \mathcal{L} described in Eq.16 is per-sample, the final loss depends on the batch size and is calculated as average across all samples.

As a way to regularize the training dataset and reduce overfitting [47], we apply mild noise augmentations to the input QPI images during training - Gaussian noise and pink (1/f) noise proved to slightly improve stability of the training and validation accuracy.

III. RESULTS

A large set of QPI images were obtained for different set of superconducting pairing functions and chemical potentials ϵ_0 , while keeping the same values of the hopping parameters t_1, \dots, t_7 (in meV) and intrinsic spin-orbit coupling parameters $\lambda_I^{(1)}$ and $\lambda_I^{(3)}$ (also in meV) to $t_1 = 33.52$, $t_2 = 97.26$, $t_3 = -2.11$, $t_4 = -13.53$, $t_5 = -10.30$, $t_6 = 3.48$, $t_7 = 1.69$, $\lambda_I^{(1)} = 13.27$, and $\lambda_I^{(3)} = -1.94$, respectively [23]. On the other hand, we have varied the chemical potential ϵ_0 values, to test whether this framework is applicable to a class of TMDC-based misfit structures [48, 49], which, despite their more complex layering, possess a band structure near the Fermi level that closely resembles that of the monolayer TMDCs, albeit with a modified chemical potential resulting from electron doping [50]. The above set of parameters fully describe the electron and the hole part of the BdG Hamiltonian; the final step is the define the allowed set of the superconducting parameters for superconducting gaps defined in Eqs. 6-11. Additionally, for all gaps in Eqs. 6-11, we have analyzed the effect of the superconducting gap intensity Δ . At the same time, this is the only free parameter to be varied in the case of superconducting gap functions that transform according to IRs A_1^u (6) and A_2^u (7), whereas in the case of gaps $\Delta_{A_1^g}$ (8) and $\Delta_{A_2^g}$ (9) there is an additional parameter $\theta \in [0, 2\pi]$ quantifying the level of singlet-triplet mixing, which was randomly sampled. Finally, we move to gap transforming to 2D IRs E^g and E^u , given in Eqs. (10) and (11). In the two case studied, besides varying the value of Δ , it is allowed to vary parameter θ , quantifying the mixing between two components of 2D IR $E^{g/u}$.

Before performing the neural network analysis, we tried to simplify the analysis by understanding the influence of free superconducting parameters on QPI images. Secondly, we note that QPI images are insensitive on the sign of the gap function, suggesting that, independently on the IR μ , gaps $\Delta_{\mu,\mathbf{k}}$ and $-\Delta_{\mu,\mathbf{k}}$ are indistinguishable. Taking this into the account, it is clear that we can restrict ourselves to a restricted range of allowed superconducting parameters: positive Δ and θ , ranging from 0 to π , instead from 0 to 2π , since $\theta \rightarrow \theta + \pi$ change induces a sign change of $\Delta_{\mu,\mathbf{k}}$, which is indistinguishable

Table I. *Evaluation metrics for detecting superconducting pairings.* For each IR (with A_1^u and A_2^u merged into a single class A_{12}^u as explained in the main text), we report the percentage probability of correctly identifying the superconducting pairing transforming according to each IR, followed by the mean absolute errors for the continuous parameters Δ , θ , and ϵ_0 of the BdG Hamiltonian (2).

IR	hit [%]	$\delta\Delta$ [meV]	$\delta\theta$ [rad]	$\delta\epsilon_0$ [eV]
A_1^g	86	0.01	0.30	0.07
A_{12}^u	94	0.01	/	0.01
A_2^g	98	0.01	0.06	0.02
E^g	98	0.01	0.01	0.01
E^u	96	0.01	0.05	0.01

by QPI imaging. Additionally, our analysis of the QPI patterns indicates that it is not possible to properly determine $\varphi(\varphi_s)$ using (time-reversal conserving) scalar impurities. Precisely this fact motivated us to use Eqs. (10) and (11) in which $\varphi(\varphi_s)$ is neglected and suggests that (time-reversal breaking) magnetic impurities should be employed instead. We leave this investigation for future work.

Finally, we notice that the QPI signatures for $\Delta_{A_1^u,\mathbf{k}}$ and $\Delta_{A_2^u,\mathbf{k}}$ become indistinguishable for the same underlying parameters in our setup. This can be traced back to the fact that, within the present modeling, the impurity effectively probes a gap opening predominantly at the Fermi level (we used $\omega = 0$ in Eq. 12) rather than symmetrically above/below it (nonzero ω), where the differences between gap functions $\Delta_{A_1^u,\mathbf{k}}$ and $\Delta_{A_2^u,\mathbf{k}}$ are the most pronounced. We therefore merge A_{1u} and A_{2u} into a single class during training and evaluation (we will call this class A_{12u} and leave the analysis of different ω for future work(s)).

We now turn to the results of the machine-learning based analysis of the QPI data. As discussed in Section II C, we evaluate the trained network by measuring (i) the representation hit rate, defined as the fraction of samples with a given ground-truth IR for which the predicted IR (argmax over $\hat{\mathbf{p}}$) matches the label, and (ii) the mean absolute error (MAE) for each regressed parameter within each ground-truth IR subset. For the mixing angle, the MAE is computed after reconstructing θ from $(\sin 2\theta, \cos 2\theta)$, respecting the π -periodicity.

Table I summarizes the per-representation performance metrics for detecting superconducting pairings, including classification probabilities and MAE for Δ , θ , and μ . Overall, the model achieves near-perfect recognition for most IRs, while the reduced hit rate for A_1^g and E^u reflects the intrinsically weaker and/or more ambiguous QPI signatures available to a scalar impurity in these cases. This represents the main result of our work: machine learning can detect different superconducting pairing symmetries with very high success rates—even using scalar impurities and a single excitation energy

($\omega = 0$)—paving the way for precise identification of pairing functions in quantum materials like monolayer NbSe₂.

A second important result is that the trained neural network is able to recognize superconducting parameters of the BdG Hamiltonian [51]: the regression errors $\delta\Delta$ remain small for the gap magnitude Δ across all IRs, indicating that Δ leaves a robust imprint on the QPI patterns. Additionally, once the $\theta \equiv \theta + \pi$ ambiguity is resolved via the $(\sin 2\theta, \cos 2\theta)$ embedding, the trained network reliably determines the presence of the singlet-triplet (component) mixing; however, the precision of obtaining the exact θ parameter differs among different IRs. The same IR dependence on the precision of the chemical potential value is evident from the results in Table I; nonetheless, these values can be meaningfully compared to those extracted via first-principles calculations combined with tight-binding modeling.

IV. CONCLUSIONS

We introduced a machine-learning protocol that infers superconducting pairing symmetries and order parameters directly from simulated quasiparticle interference images of monolayer NbSe₂. By training a two-head convolutional neural network, we simultaneously identified the type of the superconducting pairing function, classified according to the irreducible representation of the \mathbf{D}_{3h} group, and continuous parameters of the superconducting state, including singlet–triplet mixing and the gap magnitude. Regularization through carefully chosen input augmentations yields models that remain robust under experiment-like noise conditions.

Our results show that the QPI-to-parameter inverse problem is tractable with high accuracy for most symmetry channels, even within a minimal scalar Anderson-impurity description and at a single excitation energy. At the same time, they expose intrinsic limitations of this framework: certain representations (notably A_1^u and A_2^u) are effectively degenerate in their QPI response and are best treated as a merged class, and the time-reversal breaking nature of superconducting pairing functions transforming according to two-dimensional irreducible representations cannot be resolved within the scalar impurity model.

These insights establish a concrete route toward symmetry- and parameter-resolved analysis of QPI data in unconventional superconductors and highlight clear extensions of the framework—such as incorporating magnetic and orbital-selective impurity channels, energy-resolved QPI, or more realistic tunneling matrix elements—to further lift degeneracies and enhance identifiability in multi-component pairing states.

ACKNOWLEDGMENTS

A.H. acknowledges the financial support provided by the Ministry of Education, Research, Development and Youth of the Slovak Republic, provided under Grant numbers APVV-21-0272 and VEGA 2/0133/25. M.G. acknowledges financial support provided by the Ministry of Education, Research, Development and Youth of the Slovak Republic, provided under Grant No. VEGA 1/0104/25 and the Slovak Academy of Sciences project IMPULZ IM-2021-42, and support of the QM4ST project funded by Programme Johannes Amos Comenius, call Excellent Research (Project No. CZ.02.01.01/00/22_008/0004572). M.M. acknowledges the financial support by the EU NextGenerationEU through the Recovery and Resilience Plan for Slovakia under the Project No. 09I02-03-V01-00012, by the APVV grant APVV-23-0430, and VEGA grants 2/0081/26 and 2/0133/25.

DATA AVAILABILITY STATEMENT

The quasiparticle interference datasets generated and analyzed during the current study (total size ≈ 50 GB) are not publicly archived due to their volume, but are available from the corresponding author on reasonable request.

Appendix A: Superconducting gap function

Here, we provide a set of allowed superconducting gap function that can be constructed in a single-band approximation for a free-standing NbSe₂ monolayer, having a \mathbf{D}_{3h} symmetry. The procedure for obtaining all symmetry allowed superconducting gap functions is equivalent to the case defined in [23], albeit different symmetry group is imposed, the one of a freestanding NbSe₂ monolayer, not of NbSe₂ on a substrate.

Superconducting pairing function can be classified according to the IRs of the \mathbf{D}_{3h} group: four one-dimensional IRs A_1^g , A_1^u , A_2^g , A_2^u , and two two-dimensional IRs E^g and E^u . Note that labels g and u represent parity quantum number with respect to the horizontal mirror plane symmetry σ_h . As mentioned in the main text, it is additionally possible to classify superconducting pairing functions into one singlet (s) and two distinct triplet channels (t, z) and (t, xy). Each of the pairing channels are characterized by the appropriate spin functions: $d_0 = i\sigma_y\sigma_0$ for singlet, $d_z = i\sigma_y\sigma_z$ for (t, z) and $(d_x, d_y) = (i\sigma_y\sigma_x, i\sigma_y\sigma_y)$ for (t, xy) spin triplet channel.

Whereas in the case of 1D IRs superconducting pairing function is uniquely determined by a single function,

we will call it $\Delta_{A_{1/2}^{g/u}, \mathbf{k}}^{(s)/(t,z)/(t,xy)}$, whereas in the case of 2D IRs $E^{g/u}$, the general form of the gap function can be written as $\Delta_{E^{g/u}, \mathbf{k}}^c = (\cos \theta_c \Delta_{E_1^{g/u}, \mathbf{k}}^c + e^{i\varphi_c} \sin \theta_c \Delta_{E_2^{g/u}, \mathbf{k}}^c)$, $c = (s), (t, z), (t, xy)$, where $\Delta_{E_{1/2}^{g/u}, \mathbf{k}}^c$ are real functions to be constructed using the symmetry-based procedure, whereas θ_s measures the size of the mixing between the two components, while the parameter $\varphi_s \neq 0$ signals the time-reversal symmetry breaking nature of the gap function.

In the singlet case, classified using the single spinor function d_0 , nonzero gap functions belong to the IRs A_1^g , A_2^g , and E^g and their explicit \mathbf{k} -dependence is the following

$$\begin{aligned}\Delta_{A_1^g, \mathbf{k}}^{(s)} &= \left[2 \cos(k_x a) + 4 \cos \frac{k_x a}{2} \cos \frac{\sqrt{3} k_y a}{2} \right] d_0, \\ \Delta_{A_2^g, \mathbf{k}}^{(s)} &= 2 \left[\sin \frac{k_x a}{2} \sin \frac{3\sqrt{3} k_y a}{2} - \sin(2k_x a) \right. \\ &\quad \times \sin(\sqrt{3} k_y a) + \sin \frac{5k_x a}{2} \sin \frac{\sqrt{3} k_y a}{2} \left. \right] d_0, \\ \Delta_{E_1^g, \mathbf{k}}^{(s)} &= \left[\cos(k_x a) - \cos \frac{k_x a}{2} \cos \frac{\sqrt{3} k_y a}{2} \right] d_0, \\ \Delta_{E_2^g, \mathbf{k}}^{(s)} &= \left[\sqrt{3} \sin \frac{k_x a}{2} \sin \frac{\sqrt{3} k_y a}{2} \right] d_0.\end{aligned}\quad (\text{A1})$$

We note that it is not possible to construct singlet gaps that transform according to IRs A_1^u , A_2^u , and E^u due to symmetry constraints (in the case of the single-band approximation employed here, see Section II A).

Secondly, we present the explicit formulas for the triplet gap functions constructed using the d_z spinor function, classified in terms of the IRs A_1^g , A_2^g , and E^g (due to symmetry constraints, for the same reason as in the singlet case, it is not possible to construct triplet gap functions with d_z spinor that would belong to IRs A_1^u , A_2^u , and E^u)

$$\begin{aligned}\Delta_{A_1^g, \mathbf{k}}^{(t,z)} &= \left[\left(\cos \frac{k_x a}{2} - \cos \frac{\sqrt{3} k_y a}{2} \right) \sin \frac{k_x a}{2} \right] d_z, \\ \Delta_{A_2^g, \mathbf{k}}^{(t,z)} &= \left[\sin(\sqrt{3} k_y a) - 2 \sin \frac{\sqrt{3} k_y a}{2} \cos \frac{3k_x a}{2} \right] d_z, \\ \Delta_{E_1^g, \mathbf{k}}^{(t,z)} &= \left[\sin(k_x a) + \sin \frac{k_x a}{2} \cos \frac{\sqrt{3} k_y a}{2} \right] d_z, \\ \Delta_{E_2^g, \mathbf{k}}^{(t,z)} &= \left[\sqrt{3} \cos \frac{k_x a}{2} \sin \frac{\sqrt{3} k_y a}{2} \right] d_z.\end{aligned}\quad (\text{A2})$$

Again, in the case of the 2D representations the general form of the gap function can be written as $\Delta_{E^u, \mathbf{k}}^{(t,z)} = (\cos \theta_t \Delta_{E_1^u, \mathbf{k}}^{(t,z)} + e^{i\varphi_t} \sin \theta_t \Delta_{E_2^u, \mathbf{k}}^{(t,z)})$, with θ_t/φ_t measuring the component mixing/time-reversal symmetry breaking.

Finally, we present superconducting gap function con-

structed using the multiplet $(d_x, d_y) = (i\sigma_y \sigma_x, i\sigma_y \sigma_y)$

$$\begin{aligned}\Delta_{A_1^u, \mathbf{k}}^{(t,xy)} &= \left[3 \cos \frac{k_x a}{2} \sin \frac{\sqrt{3} k_y a}{2} \right] d_x - \left[\sqrt{3} \left(2 \cos \frac{k_x a}{2} \right. \right. \\ &\quad \left. \left. + \cos \frac{\sqrt{3} k_y a}{2} \right) \sin \frac{k_x a}{2} \right] d_y, \\ \Delta_{A_2^u, \mathbf{k}}^{(t,xy)} &= \left[\left(2 \cos \frac{k_x a}{2} + \cos \frac{\sqrt{3} k_y a}{2} \right) \sin \frac{k_x a}{2} \right] d_x \\ &\quad + \left[\sqrt{3} \cos \frac{k_x a}{2} \sin \frac{\sqrt{3} k_y a}{2} \right] d_y, \\ \Delta_{E_1^u, \mathbf{k}}^{(t,xy)} &= \left[2 \sin(\sqrt{3} k_y a) - \cos \frac{3k_x a}{2} \sin \frac{\sqrt{3} k_y a}{2} \right] d_x \\ &\quad + \left[\sqrt{3} \sin \frac{3k_x a}{2} \cos \frac{\sqrt{3} k_y a}{2} \right] d_y, \\ \Delta_{E_2^u, \mathbf{k}}^{(t,xy)} &= \left[\sqrt{3} \sin \frac{3k_x a}{2} \cos \frac{\sqrt{3} k_y a}{2} \right] d_x \\ &\quad - \left[3 \cos \frac{3k_x a}{2} \sin \frac{\sqrt{3} k_y a}{2} \right] d_y,\end{aligned}\quad (\text{A3})$$

classified according to the IRs A_1^u , A_2^u , and E^u ; due to symmetry constraints, no gap functions that transform according to IRs A_1^g , A_2^g , and E^g can be constructed.

In previous equations, Eqs. (A1)-(A3), we have presented all possible superconducting gaps, classified in terms of IRs of the given \mathbf{D}_{3h} group. An additional feature of this classification is the possibility to have mixed singlet-triplet components, since in the A_1^g , A_2^g , and E^g case, both singlet (s) and triplet (t, z) components are present. Taking this into account, the most general form of the gap function that transform according to 1D IRs

$$\begin{aligned}\Delta_{A_1^u, \mathbf{k}} &= \Delta \Delta_{A_1^u, \mathbf{k}}^{(t,xy)}, \\ \Delta_{A_2^u, \mathbf{k}} &= \Delta \Delta_{A_2^u, \mathbf{k}}^{(t,xy)}, \\ \Delta_{A_1^g, \mathbf{k}} &= \Delta (\cos \theta \Delta_{A_1^g, \mathbf{k}}^{(s)} + \sin \theta \Delta_{A_1^g, \mathbf{k}}^{(t,z)}), \\ \Delta_{A_2^g, \mathbf{k}} &= \Delta (\cos \theta \Delta_{A_2^g, \mathbf{k}}^{(s)} + \sin \theta \Delta_{A_2^g, \mathbf{k}}^{(t,z)}),\end{aligned}\quad (\text{A4})$$

whereas in the 2D case the most general form is equal to

$$\Delta_{E^u, \mathbf{k}} = \Delta (\cos \theta_1 \Delta_{E_1^u, \mathbf{k}}^{(t,xy)} + e^{i\varphi_1} \sin \theta_1 \Delta_{E_2^u, \mathbf{k}}^{(t,xy)}), \quad (\text{A5})$$

$$\begin{aligned}\Delta_{E^g, \mathbf{k}} &= \Delta \left[\cos \theta (\cos \theta_s \Delta_{E_1^g, \mathbf{k}}^{(s)} + e^{i\varphi_s} \sin \theta_s \Delta_{E_2^g, \mathbf{k}}^{(s)}) + \right. \\ &\quad \left. \sin \theta (\cos \theta_t \Delta_{E_1^g, \mathbf{k}}^{(t,z)} + e^{i\varphi_t} \sin \theta_t \Delta_{E_2^g, \mathbf{k}}^{(t,z)}) \right],\end{aligned}\quad (\text{A6})$$

where Δ represents the amplitude of the superconducting gap. As discussed above, in the case of the 1D IRs A_1^u and A_2^u no mixing occurs, whereas in the case of 1D IRs A_1^g and A_2^g there is only one mixing parameter. In the case of the 2D IRs the situation becomes more complicated since in the E^u case, there are two parameters included in the mixing of the two components of the same gap constructed using the d_{xy} triplet. In the second case, IR E^g , there is a mixing between the singlet and the triplet

component d_z . The total number of parameters in this case is 5, where θ represents the mixing between the singlet and the triplet component, whereas $(\theta_s, \varphi_s)/(\theta_t, \varphi_t)$ are the mixing parameters within the 2D space of the singlet/ d_z space.

In the main text, we focus on all 1D IRs A_1^u , A_1^g , A_2^u , and A_2^g (A4). To simplify our study and to prove our concept that machine learning can be used to distinguish different features of the superconductivity, we focus on the singlet component of the 2D IR E^g only (see Eq. (11)), whereas keeping $\Delta_{E^u, \mathbf{k}}$ as in Eq. (A5).

Appendix B: Architecture of the neural network

Here, we provide schematics of the neural network architecture (see Fig. 2) used to predict the type of superconducting pairing and the microscopic parameters of the BdG Hamiltonian.

REFERENCES

-
- [1] D. J. Scalapino, *Rev. Mod. Phys.* **84**, 1383 (2012).
- [2] Z. K. Liu, L. X. Yang, S.-C. Wu, C. Shekhar, J. Jiang, H. F. Yang, Y. Zhang, S.-K. Mo, Z. Hussain, B. Yan, C. Felser, and Y. L. Chen, *Nat. Commun.* **7**, 12924 (2016).
- [3] H. Kim, K. Wang, Y. Nakajima, R. Hu, S. Ziemak, P. Syers, L. Wang, H. Hodovanets, J. D. Denlinger, P. M. R. Brydon, D. F. Agterberg, M. A. Tanatar, R. Prozorov, and J. Paglione, *Science Advances* **4**, eaao4513 (2018).
- [4] R. M. Fernandes, A. V. Chubukov, and J. Schmalian, *Nat. Phys.* **10**, 97–104 (2014).
- [5] P. J. Hirschfeld, M. M. Korshunov, and I. I. Mazin, *Rep. Prog. Phys.* **74**, 124508 (2011).
- [6] S. Kashiwaya and Y. Tanaka, *Rep. Prog. Phys.* **63**, 1641 (2000).
- [7] M. P. Allan, F. Masee, D. K. Morr, J. Van Dyke, A. W. Rost, A. P. Mackenzie, C. Petrovic, and J. C. Davis, *Nat. Phys.* **9**, 468–473 (2013).
- [8] T. Hanaguri, S. Niihata, K. Kuroki, and H. Takagi, *Science* **328**, 474 (2010).
- [9] D. C. Johnston, *Adv. Phys.* **59**, 803 (2010).
- [10] J. S. Hofmann, R. Queiroz, and A. P. Schnyder, *Phys. Rev. B* **88**, 134505 (2013).
- [11] A. Kreisel, P. Choubey, T. Berlijn, W. Ku, B. M. Andersen, and P. J. Hirschfeld, *Phys. Rev. Lett.* **114**, 217002 (2015).
- [12] A. Dutt, A. A. Golubov, O. V. Dolgov, and D. V. Efremov, *Phys. Rev. B* **96**, 054513 (2017).
- [13] L. C. Rhodes, W. Osmolska, C. A. Marques, and P. Wahl, *Phys. Rev. B* **107**, 045107 (2023).
- [14] M. Zeng, X. Li, Y. Wang, and S. Feng, *Phys. Rev. B* **110**, 134523 (2024).
- [15] A. Crépieux, E. Pangburn, S. Wang, K. Zhussupbekov, J. P. Carroll, B. Hu, Q. Gu, J. C. S. Davis, C. Pépin, and C. Bena, *Phys. Rev. B* **112**, 214509 (2025).
- [16] L. Engström, P. Simon, and A. Mesaros, *Phys. Rev. B* **111**, 134505 (2025).
- [17] M. F. Crommie, C. P. Lutz, and D. M. Eigler, *Nature* **363**, 524 (1993).
- [18] P. T. Sprunger, L. Petersen, E. W. Plummer, and E. Lægsgaard, *Science* **275**, 1764 (1997).
- [19] P. Hofmann, B. G. Briner, M. Doering, H.-P. Rust, E. W. Plummer, and A. M. Bradshaw, *Phys. Rev. Lett.* **79**, 265 (1997).
- [20] N. Levy, T. Zhang, J. Ha, F. Sharifi, A. A. Talin, Y. Kuk, and J. A. Stroscio, *Phys. Rev. Lett.* **110**, 117001 (2013).
- [21] H. Kim, Y. Choi, C. Lewandowski, A. Thomson, Y. Zhang, R. Polski, K. Watanabe, T. Taniguchi, J. Alicea, and S. Nadj-Perge, *Nature* **606**, 494–500 (2022).
- [22] S. Wang, K. Zhussupbekov, J. P. Carroll, B. Hu, X. Liu, E. Pangburn, A. Crépieux, C. Pépin, C. Broyles, S. Ran, N. P. Butch, S. Saha, J. Paglione, C. Bena, J. C. S. Davis, and Q. Gu, *Nature Physics* **21**, 1555–1562 (2025).
- [23] J. Haniš, M. Milivojević, and M. Gmitra, *Phys. Rev. B* **110**, 104502 (2024).
- [24] Y. LeCun, Y. Bengio, and G. Hinton, *Nature* **521**, 436–444 (2015).
- [25] J. Gu, Z. Wang, J. Kuen, L. Ma, A. Shahroudy, B. Shuai, T. Liu, X. Wang, G. Wang, J. Cai, and T. Chen, *Pattern Recognit.* **77**, 354 (2018).
- [26] Y. Zhang, A. Mesaros, K. Fujita, S. D. Edkins, M. H. Hamidian, K. Ch’ng, H. Eisaki, S. Uchida, J. C. Séamus Davis, E. Khatami, and E.-A. Kim, *Nature* **570**, 484–490 (2019).
- [27] G. E. Volovik and L. P. Gor’kov, *Zh. Eksp. Teor. Fiz.* **88**, 1412 (1985).
- [28] S.-O. Kaba and D. Sénéchal, *Phys. Rev. B* **100**, 214507 (2019).
- [29] C.-w. Cho, J. Lyu, L. An, T. Han, K. T. Lo, C. Y. Ng, J. Hu, Y. Gao, G. Li, M. Huang, N. Wang, J. Schmalian, and R. Lortz, *Phys. Rev. Lett.* **129**, 087002 (2022).
- [30] S. Hörhold, J. Graf, M. Marganska, and M. Grifoni, *2D Mater.* **10**, 025008 (2023).
- [31] J. Siegl, A. Bleibaum, W. Wan, M. Kurpas, J. Schliemann, M. M. Ugeda, M. Marganska, and M. Grifoni, *Nat. Commun.* **16**, 8228 (2025).
- [32] X. Lu and D. Sénéchal, *Phys. Rev. B* **98**, 245118 (2018).
- [33] D. Sticlet and C. Morari, *Phys. Rev. B* **100**, 075420 (2019).
- [34] J. M. Byers, M. E. Flatté, and D. J. Scalapino, *Phys. Rev. Lett.* **71**, 3363 (1993).
- [35] J. Hoffman, K. McElroy, D.-H. Lee, K. Lang, H. Eisaki, S. Uchida, and J. Davis, *Science* **297**, 1148 (2002).
- [36] T. Pereg-Barnea and M. Franz, *Phys. Rev. B* **68**, 180506 (2003).
- [37] T. S. Nunner, W. Chen, B. M. Andersen, A. Melikyan, and P. J. Hirschfeld, *Phys. Rev. B* **73**, 104511 (2006).
- [38] W. Chen, C. Neerup Breið, F. Masee, M. P. Allan, C. Petrovic, J. C. S. Davis, P. J. Hirschfeld, B. M. Andersen, and A. Kreisel, *Nat. Commun.* **14**, 2984 (2023).
- [39] L. Capriotti, D. J. Scalapino, and R. D. Sedgewick, *Phys. Rev. B* **68**, 014508 (2003).
- [40] L. Zhu, W. Atkinson, and P. Hirschfeld, *Phys. Rev. B* **69**, 060503 (2004).
- [41] E. N. Economou, *Green’s functions in quantum physics*, Vol. 7 (Springer Science & Business Media, 2006).

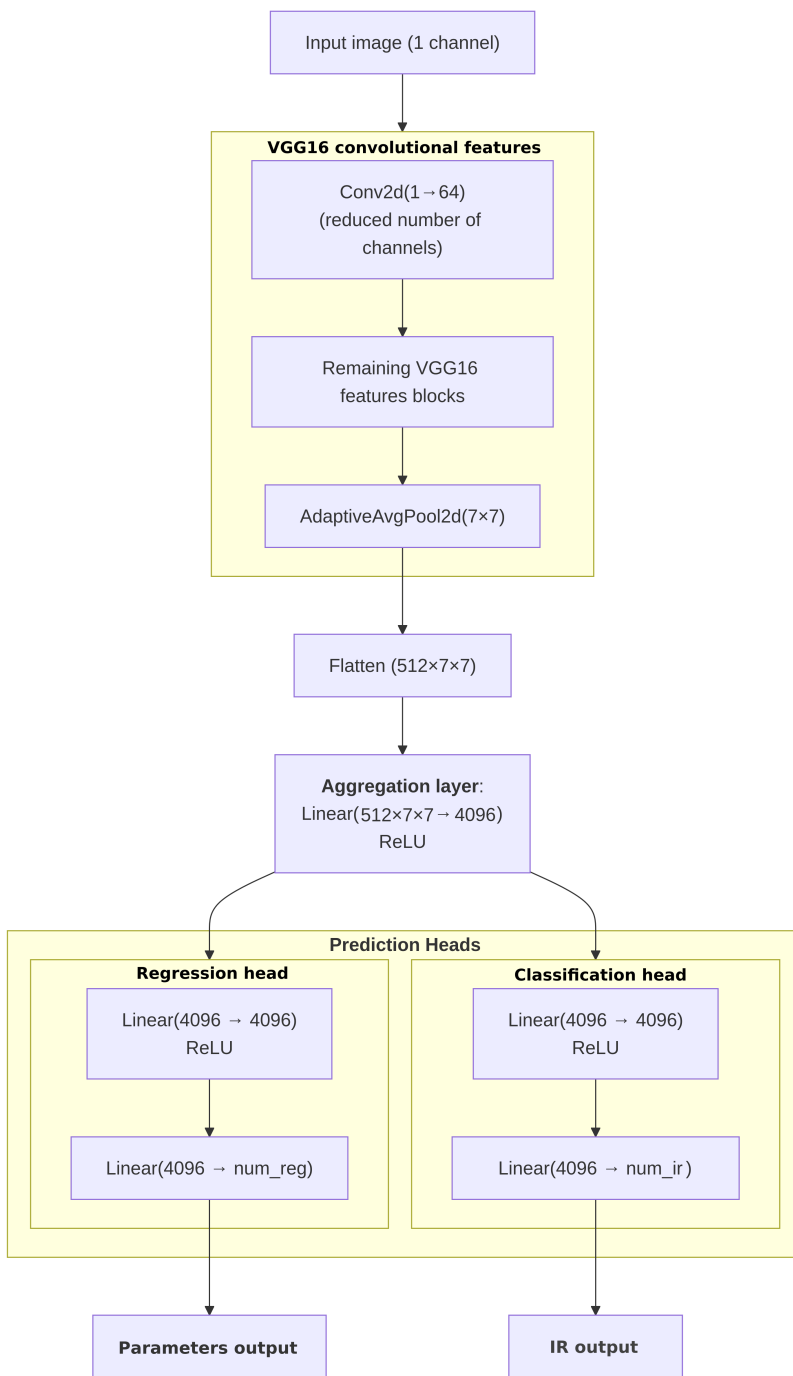


Figure 2. *Architecture of the neural network.* The model is based on VGG16 [43, 44] architecture, input channels reduced from 3 to 1, prediction head replaced with two custom prediction heads, one for classification (IRs), the other one for regression (parameters).

- [42] Y. Kohsaka, T. Machida, K. Iwaya, M. Kanou, T. Hanaguri, and T. Sasagawa, *Phys. Rev. B* **95**, 115307 (2017).
- [43] K. Simonyan and A. Zisserman, [arXiv:1409.1556](https://arxiv.org/abs/1409.1556) (2014).
- [44] X. Ding, X. Zhang, N. Ma, J. Han, G. Ding, and J. Sun, [arXiv:2101.03697](https://arxiv.org/abs/2101.03697) (2021).
- [45] K. He, X. Zhang, S. Ren, and J. Sun, in *2015 IEEE International Conference on Computer Vision (ICCV)* (2015) pp. 1026–1034.
- [46] Z. Liu, H. Mao, C.-Y. Wu, C. Feichtenhofer, T. Darrell, and S. Xie, Proceedings of the IEEE/CVF Conference on Computer Vision and Pattern Recognition (CVPR) (2022).
- [47] C. M. Bishop, *Neural Computation* **7**, 108 (1995).
- [48] R. Roesky, A. Meerschaut, J. Rouxel, and C. J., *Z. Anorg. Allg. Chem.* **619**, 117 (1993).

- [49] A. Nader, A. Lafond, A. Briggs, A. Meerschaut, and R. Roesky, *Synth. Met.* **97**, 147 (1998).
- [50] R. T. Leriche, A. Palacio-Morales, M. Campetella, C. Tresca, S. Sasaki, C. Brun, F. Debontridder, P. David, I. Arfaoui, O. Šofranko, T. Samuely, G. Kremer, C. Monney, T. Jaouen, L. Cario, M. Calandra, and T. Cren, *Adv. Funct. Mater.* **31**, 2007706 (2020).
- [51] M. Khosravian, R. Koch, and J. L. Lado, *J. Phys. Mater.* **7**, 015012 (2024).